

Carbon-Oxygen Phase Separation in MESA White Dwarf Models

EVAN B. BAUER ¹

¹*Center for Astrophysics | Harvard & Smithsonian, 60 Garden St, Cambridge, MA 02138, USA*

ABSTRACT

We enhance the treatment of crystallization for models of white dwarfs (WDs) in the stellar evolution software MESA by implementing carbon-oxygen (C/O) phase separation. The phase separation process during crystallization leads to transport of oxygen toward the center of WDs, resulting in a more compact structure that liberates gravitational energy as additional heating that modestly slows WD cooling timescales. We quantify this cooling delay in MESA C/O WD models over the mass range $0.5 - 1.0 M_{\odot}$, finding delays of $0.5 - 0.8$ Gyr for typical C/O interior profiles. MESA WD cooling timescales including this effect are generally comparable to other WD evolution models that make similar assumptions about input physics. When considering phase separation alongside ^{22}Ne sedimentation, however, we find that both MESA and BaSTI WD cooling models predict a more modest sedimentation delay than the latest LPCODE models, and this may therefore require a re-evaluation of previously proposed solutions to some WD cooling anomalies that were based on LPCODE models of ^{22}Ne sedimentation. Our implementation of C/O phase separation in the open-source stellar evolution software MESA provides an important tool for building realistic grids of WD cooling models, as well as a framework for expanding on our implementation to explore additional physical processes related to phase transitions and associated fluid motions in WD interiors.

Keywords: White dwarf stars (1799), Stellar physics (1621)

1. INTRODUCTION

White dwarf stars (WDs) cool over long timescales governed by the thermodynamics of their interior heat reservoirs, mediated by the physics of heat transport through their outer envelopes (Mestel 1952). With detailed WD models, these cooling timescales can be calculated accurately and used to constrain the ages of individual WDs and stellar populations that they are associated with (Winget et al. 1987; Fontaine et al. 2001). Discrepancies between WD cooling ages and independent age measurements can also be used to learn about the physical process operating in the dense plasma mixtures of WD interiors (e.g., García-Berro et al. 2010; Cheng et al. 2019; Bauer et al. 2020; Blouin et al. 2021). Several WD evolution codes attempt to implement the most up-to-date input physics and methods to provide grids of models with accurate WD cooling timescales (e.g., Camisassa et al. 2016; Bédard et al. 2020, 2022; Salaris et al. 2022; Jermyn et al. 2023).

One important physical process that can modify WD cooling timescales is the first-order phase transition of the carbon-

oxygen (C/O) mixtures in WD cores from liquid to solid when they cool to the point of crystallization (van Horn 1968; Winget et al. 2009). The latent heat associated with this phase transition can temporarily slow WD cooling, and phase separation into O-enriched solid material and C-enriched liquid mantle material can induce mixing that also impacts WD interior thermodynamics and further delays WD cooling (Stevenson 1977; Mochkovitch 1983; Segretain & Chabrier 1993; Horowitz et al. 2010; Blouin et al. 2020a).

The physics of crystallization and C/O phase separation should be included in detailed WD cooling models, and recent observations have also motivated further investigation of other phenomenology that may be tied to the physics of dense multi-component fluids. The fluid motions in the liquid mantles of crystallizing WDs have recently been proposed as a candidate mechanism for generating dynamos in some magnetic WDs (Isern et al. 2017; Ginzburg et al. 2022). While a body of observational evidence seems to support this proposal (Belloni et al. 2021; Schreiber et al. 2021b,a, 2022), recent numerical simulations have called into question whether the fluid motions are adequate to produce the necessary dynamo effect (Fuentes et al. 2023). The observed cooling anomaly for massive crystallizing WDs on the “Q-branch” (Cheng et al. 2019; Bauer et al. 2020; Camisassa

et al. 2021) has also spurred recent investigation of previously unexplored phenomena associated with impurities affecting the phase diagrams of dense plasma mixtures (Caplan et al. 2020; Blouin et al. 2021; Blouin & Daligault 2021b; Horowitz & Caplan 2021; Caplan et al. 2023).

This context motivates providing an implementation of C/O phase separation in the open-source stellar evolution software instrument MESA (Paxton et al. 2011, 2013, 2015, 2018, 2019; Jermyn et al. 2023) to aid in exploring the variety of phenomena associated with WD crystallization and mantle mixing as new observations continue to motivate more detailed investigations with stellar evolution models. MESA already includes state-of-the-art capabilities for many aspects of WD evolution, including the Skye EOS (Jermyn et al. 2021) that includes crystallization and latent heat, and ^{22}Ne sedimentation that can independently delay WD cooling (Paxton et al. 2018; Bauer et al. 2020) with the diffusion coefficients of Caplan et al. (2022) that are accurate for dense, strongly-coupled liquid plasmas. In this work, we further enhance the available physics capabilities for MESA WD models by providing an implementation of C/O phase separation based on the recent phase diagram of Blouin & Daligault (2021a).

We begin by briefly describing the setup for our MESA models and key pieces of input physics in Section 2. Section 3 then gives a detailed description of our method for implementing C/O phase separation in MESA, and shows how this implementation results in changes to interior composition profiles and heating that delays WD cooling. Section 4 shows the impact that C/O phase separation has on WD cooling timescales in MESA models, and compares to other commonly used WD cooling models. Section 5 then explores the interplay between cooling delays from both C/O phase separation and ^{22}Ne sedimentation in models descended from solar-metallicity progenitors where both effects are significant. We find important differences between MESA models and other commonly used WD cooling models when including ^{22}Ne sedimentation, and we suggest that our models require new input physics to resolve important WD cooling discrepancies such as the WD Q -branch and the WD luminosity function of NGC 6791. This motivates further work to explore stellar evolution models that include the physics of multi-component phase diagrams that account for impurities altering the C/O phase separation process, which our work here lays the groundwork for pursuing with MESA in the future.

2. CODE AND INPUT PHYSICS

Our MESA models presented in this work rely on the development version of MESA, commit 59ed280, which is publicly available on the `main` branch of the MESA GitHub

repository.¹ In most respects, this version functions very similarly to the most recent public release of MESA as of the writing of this work, r22.11.1. The C/O phase separation capabilities that are presented in this work are available on the `main` branch of the development version of MESA and will therefore be available in the next public release version of MESA after r22.11.1. A repository of work directories containing MESA input files needed to reproduce all of the models presented in this work is available on Zenodo: [doi:10.5281/zenodo.7742475](https://doi.org/10.5281/zenodo.7742475).

Radiative opacities are primarily from OPAL (Iglesias & Rogers 1993, 1996), with low-temperature data from Ferguson et al. (2005) and the high-temperature, Compton-scattering dominated regime by Poutanen (2017). Electron conduction opacities are from Cassisi et al. (2007) and Blouin et al. (2020b). Nuclear reaction rates are from JINA REACLIB (Cyburt et al. 2010), NACRE (Angulo et al. 1999) and additional tabulated weak reaction rates Fuller et al. (1985); Oda et al. (1994); Langanke & Martínez-Pinedo (2000). Screening is included via the prescription of Chugunov et al. (2007). Thermal neutrino loss rates are from Itoh et al. (1996).

The MESA equation of state (EOS) is a blend of the OPAL (Rogers & Nayfonov 2002), SCVH (Saumon et al. 1995), FreeEOS (Irwin 2004), HELM (Timmes & Swesty 2000), PC (Potekhin & Chabrier 2010), and Skye (Jermyn et al. 2021) EOSes. In particular, the Skye EOS covers the region of high density where crystallization occurs in WD interiors. Skye includes the latent heat generated by crystallizing material (Jermyn et al. 2021), and since the thermodynamics account for the full composition vector, Skye can also be used to capture the heating associated with composition changes in a WD interior during the phase separation process, as we will describe in detail in later sections.

3. PHASE SEPARATION IMPLEMENTATION

For a crystallizing C/O mixture in a WD interior, the boundary between liquid and solid has a discontinuous composition profile, with the solid interior enriched in O relative to the surrounding C/O liquid. A fluid element undergoing this transition minimizes the free energy by separating into O-enriched solid and C-enriched liquid components that are in equilibrium at the phase boundary (Stevenson 1977; Segretain & Chabrier 1993; Horowitz et al. 2010; Medin & Cumming 2010; Blouin et al. 2020a). This extrusion of C into the liquid immediately surrounding the crystallized core then excites fluid instability that leads to mixing in the liquid layers, which releases heat associated with the changing composition profile and slows the cooling of the WD, with an overall delay on the order of up to ≈ 1 Gyr (Mochkovitch 1983; Isern

¹ <https://github.com/MESAHub/mesa>

et al. 1997; Montgomery et al. 1999; Althaus et al. 2012). In this section, we provide a detailed description of the steps we have implemented in MESA to account for these effects and their influence on WD cooling timescales.

3.1. Phase Diagram at the Boundary

The phase transition occurs when the temperature falls to a point where the free energy of the solid phase is lower than the free energy of the liquid phase. Skye calculates all thermodynamics self-consistently from derivatives of the Helmholtz free energy F , and therefore has direct access to the free energy information needed to evaluate where the phase transition occurs in a C/O plasma mixture (Jermyn et al. 2021). Skye evaluates the free energy for both liquid and solid phases, and selects the phase that minimizes the free energy. The liquid-solid phase boundary is a first-order phase transition, with continuous free energy at the boundary but discontinuous derivatives resulting in discontinuities in thermodynamic quantities such as entropy $s = -(\partial F / \partial T)_\rho$.

The latent heat of crystallization is encoded in the entropy discontinuity at the phase boundary, but a sharp discontinuity is difficult to capture with the numerical methods of stellar evolution codes such as MESA. Skye therefore introduces a narrow smoothing of the entropy discontinuity at the phase transition to capture the latent heat in a continuous manner convenient for inclusion in stellar evolution codes. Skye accomplishes this by defining a continuous `phase` parameter ϕ constructed as follows. Denote the free energy of the ion mixture as $f_i = \min(f_{i,\text{liquid}}, f_{i,\text{solid}})$, where f is given in dimensionless units of free energy per $k_B T$ per ion. With the difference between the free energy of the liquid phase and solid phase $\Delta f \equiv f_{i,\text{liquid}} - f_{i,\text{solid}}$, the `phase` parameter is then constructed as

$$\phi = \frac{e^{\Delta f/w}}{e^{\Delta f/w} + 1}, \quad (1)$$

where $w = 10^{-2}$ is chosen as the blurring parameter to introduce a narrow but continuous `phase` variable that transitions from 0 to 1 when f_i is within a few percent of its value at the location of the phase transition. The phase transition from liquid to solid is located at $\phi = 0.5$, with $\phi < 0.5$ being liquid material and $\phi > 0.5$ being solid material. The latent heating term can then be constructed from a continuous smoothed entropy evaluated by taking the derivative of

$$f_{i,\text{smooth}} \equiv (1 - \phi)f_{i,\text{liquid}} + \phi f_{i,\text{solid}}. \quad (2)$$

For more details see section 3 of Jermyn et al. (2021).²

We therefore use the thermodynamics and phase information reported by the Skye EOS in our MESA models to deter-

mine when the fluid in a cooling WD has reached the point of crystallization, along with the resulting latent heat released by the ensuing phase transition. In terms of the plasma coupling parameter $\Gamma \equiv e^2 \langle Z^5/3 \rangle / a_e k_B T$ (where Z is ion charge and a_e is average electron spacing), Jermyn et al. (2021) show that the crystallization in a C/O mixture according to Skye occurs around $\Gamma \approx 200 - 230$ depending on C/O ratio, generally in good agreement with other state-of-the-art C/O phase curves such as those of Horowitz et al. (2010), Blouin et al. (2020a), and Blouin & Daligault (2021a). For our models throughout this paper, we specifically use Skye with the Ogata et al. (1993) option for the solid mixing term of the free energy, along with the options to extrapolate the thermodynamic fits near the phase transition. This gives a crystallization temperature within a few percent of the liquidus of the Blouin et al. (2020a) phase diagram for C/O mixtures (figure 8 of Jermyn et al. 2021, “fits extended” lower panel).

In principle, Skye could also be used to solve the double-tangent optimization problem for separating the C/O composition into the solid and liquid components that minimize the free energy (Medin & Cumming 2010). However, for the composition changes due to phase separation at the boundary, we instead elect to use the phase diagram of Blouin & Daligault (2021a). Specifically, we use the fitting form given by equation (34) and Table II of that work.

The temperature profile in the core of a cooling WD is nearly isothermal, so crystallization starts at the center where ρ and Γ are highest. We begin the process of phase separation when the model cools to a point where the phase in the central zone of the model passes $\phi > \phi_{\text{sep}}$. While the first-order phase transition formally occurs precisely at $\phi = 0.5$ by construction (Eqn 1, $\Delta f = 0$), we offset the location of the phase separation induced composition discontinuity slightly further into the solid phase by choosing $\phi_{\text{sep}} = 0.9$ to avoid having phase separation interfere with the release of the smoothed latent heat term. This is because the method for including the latent heat in Skye relies on density and temperature evolution, and does not account for composition changes (Jermyn et al. 2021). For an individual fluid element to release all the latent heat associated with evolving through the phase transition in Skye, it needs to evolve continuously through ϕ near 0.5. Phase separation causes a composition discontinuity that also causes ϕ to evolve discontinuously, as seen in Figure 1. This figure shows the latent heat in MESA WD models undergoing both crystallization and phase separation according to our procedure using the Skye EOS. Fluid elements evolve continuously from left to right in this figure as they cool at nearly constant density, except where the composition discontinuity from phase separation causes a discontinuous jump to higher ϕ and Γ shown by the dotted lines in the figure.

² Note that equation (41) in Jermyn et al. (2021) has a typo in its definition of $f_{i,\text{smooth}}$, which is why it does not agree exactly with Eqn (2) here.

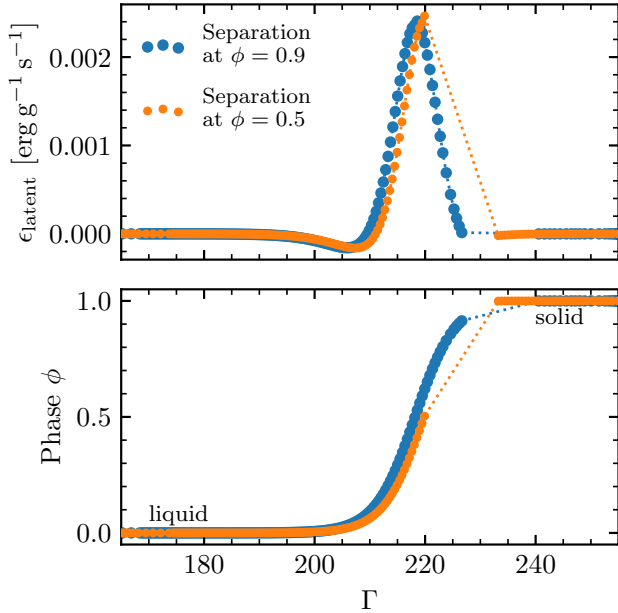


Figure 1. Latent heat and phase profiles as a function of plasma coupling Γ for WD models undergoing both crystallization and phase separation using the Skye EOS. Points represent zones in the discretized stellar model, connected by thin dotted lines showing where the phase separation composition discontinuity lies.

The latent heat is strongly peaked at the location of the phase transition from liquid to solid at $\phi = 0.5$, which occurs at $\Gamma \approx 218$ in the C/O WD model used for Figure 1 according to Skye. In the model where we impose phase separation precisely at $\phi = 0.5$, the composition discontinuity at that location causes fluid elements to skip discontinuously past some of the latent heating near the peak, causing some heat to be missed in the model. For the model where we slightly delay phase separation to $\phi = 0.9$, the composition discontinuity is slightly offset into the solid phase at $\Gamma \approx 226$ and therefore does not impact the latent heat distribution in this model. Offsetting the composition changes due to phase separation toward the solid side of the phase transition allows each fluid element first to release the smoothed latent heat of crystallization and then undergo phase separation.

A fluid element evolves through $\phi = 0.9$ very soon after $\phi = 0.5$ because of the narrow blurring parameter w , so any heat release associated with phase separation will occur with only minimal delay and will not effect any resulting cooling delay introduced into the overall WD evolution. Figure 2 shows that in the center of a crystallizing WD model, ϕ evolves from 0.5 to 0.9 while the luminosity of the WD changes by only about $\Delta \log L_{\text{WD}} \approx 0.04$, or about 10%. This ensures that any heating associated with phase separation and associated mixing will occur only slightly later due to moving phase separation to $\phi = 0.9$. The slightly lower luminosity at which the phase separation energy is released means that

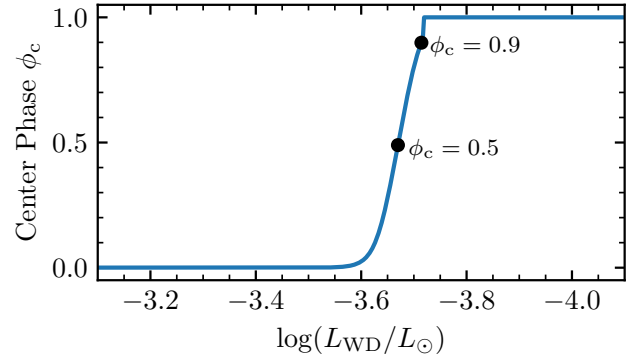


Figure 2. Evolution of the center phase ϕ_c as a function of WD luminosity for a cooling and crystallizing WD model.

a cooling delay could be overestimated, but by no more than about 10%. Greater precision would simply require higher resolution models and an even smaller blurring parameter $w < 10^{-2}$ to make the smoothed phase transition and latent heat peak more strongly about the location of $\phi = 0.5$, so that ϕ_{sep} could be moved closer to the location of the phase transition at $\phi = 0.5$.

To summarize, as a mass coordinate in a WD interior cools and evolves toward crystallization, we determine when it has reached the point of crystallization from the thermodynamic and phase information reported by the Skye EOS (Jermyn et al. 2021), and we adjust the composition at the phase boundary using the C/O phase separation diagram of Blouin & Daligault (2021a).

3.2. Separation, Fluid Instability, and Mixing

Here we describe the iterative procedure for propagating the crystallization front and associated phase separation discontinuity outward from the center of the model as the WD cools, along with the associated mixing in the liquid mantle immediately surrounding the solid core.

We label the discrete grid cells of a MESA model by zone number $k = 1, \dots, N_z$, with $k = 1$ for the surface zone and $k = N_z$ for the central zone (so that zone $k-1$ is the zone immediately outward from zone k). We track the mass coordinate m_{cr} of the boundary between the crystallized solid material and surrounding liquid. We assume that this starts at $m_{\text{cr}} = 0$ where density is highest in a WD, and m_{cr} then evolves monotonically toward larger values as the WD cools. We update and save this value between evolution steps to track which material is newly crystallized (and therefore undergoing phase separation) in a given time step. With m_{cr} therefore encoding the last known location of the solid core boundary, we iterate outward starting from the core boundary by starting at the largest k such that the mass coordinate m_k of that zone satisfies $m_k > m_{\text{cr}}$. If $\phi_k > \phi_{\text{sep}}$, then zone k must undergo C/O phase separation during the time step, so we adjust its

composition by enriching the oxygen mass fraction in zone k by

$$X_{O,k} \rightarrow X_{O,k} + \Delta X_{O,k}, \quad (3)$$

where $\Delta X_{O,k}$ is calculated as a function of $X_{O,k}$ using the fit of [Blouin & Daligault \(2021a\)](#). Conservation of mass requires that we also adjust the carbon mass fraction in zone k by

$$X_{C,k} \rightarrow X_{C,k} - \Delta X_{O,k}. \quad (4)$$

This enrichment of O in zone k extrudes C into zone $k-1$ to compensate and conserve elements. Since adjacent cells may span different amounts of mass depending on the mesh scheme of the model, we must account for the mass δm_k contained in zone k relative to the mass δm_{k-1} contained in zone $k-1$ to properly conserve the amount of C/O mixed between the two cells. The mass fractions of C and O in zone $k-1$ must therefore be adjusted by

$$X_{C,k-1} \rightarrow X_{C,k-1} + \Delta X_{O,k} \delta m_k / \delta m_{k-1}, \quad (5)$$

and

$$X_{O,k-1} \rightarrow X_{O,k-1} - \Delta X_{O,k} \delta m_k / \delta m_{k-1}. \quad (6)$$

After making these composition adjustments, we mark zone k as having crystallized by advancing m_{cr} to the mass coordinate of the outer edge of zone k ($m_{\text{cr}} \rightarrow m_{\text{cr}} + \delta m_k$).

Note that the C/O phase curves used for phase separation are calculated assuming pure C/O mixtures, so for a WD model with other trace metals present (e.g. Ne) we simplify by assuming that the other traces are inert and unaffected at the phase boundary. We rescale the C and O mass fractions up proportionally such that $X_{C/O} = X_C + X_O = 1$, perform the phase separation composition adjustments at the boundary, and then scale the compositions back down to reach the original value of $X_{C/O}$, while leaving the mass fractions of other trace elements unchanged.

After advancing the core boundary through zone k , the fluid in the surrounding zone $k-1$ is generally depleted of heavier O and enriched in C relative to its surroundings according to Eqns (5)–(6), leaving the model with an inverted molecular weight gradient just outside the core boundary. This can excite dynamical instability that mixes the liquid outward ([Mochkovitch 1983](#); [Ginzburg et al. 2022](#)). This dynamical mixing takes place on a timescale much shorter than the stellar evolution time steps that we take for WD cooling, so we approximate this mixing as an efficient process that fully mixes material outward until the composition profile re-establishes stability, following a procedure similar to “convective pre-mixing” described in [Paxton et al. \(2019\)](#).

We quantify instability leading to dynamical mixing in terms of the Ledoux criterion for convection

$$\nabla_T > \nabla_{\text{ad}} + B, \quad (7)$$

where ∇_{ad} is the local adiabatic temperature gradient reported by the EOS, $B \propto \nabla_{\mu}$ is the Ledoux term accounting for the composition gradient as constructed in [Paxton et al. \(2013\)](#) (∇_{μ} is the molecular weight gradient), and ∇_T is the actual temperature gradient in the model. In practice, the temperature gradient in a WD interior is negligible due to efficient electron conduction, so this criterion for instability often reduces to $|B| \gtrsim \nabla_{\text{ad}}$ (note that $B < 0$ in the context of phase separation, where the inverted molecular weight gradient from C enrichment in the mantle acts to excite dynamical instability). After advancing the crystallization boundary through zone k , we iterate outward starting in zone $k-1$, fully mixing the contents of N zones $k-1, \dots, k-N$ until the resulting composition gradient becomes shallow enough that Eqn (7) is no longer satisfied in zone $k-N$ and stability is achieved.

The composition adjustments in the preceding steps are made at constant P and T to maintain hydrostatic equilibrium, and we use Skye to update the EOS quantities for affected zones after both phase separation and mantle mixing composition changes. After these EOS updates, the crystallized side of the boundary generally moves further into the solid phase $\phi_k > \phi_{\text{sep}}$ due to O enrichment increasing Γ at fixed T . We then check whether $\phi_{k-1} > \phi_{\text{sep}}$ so that crystallization must continue advancing through zone $k-1$ as well. If so, we repeat the preceding steps, separating so that zone $k-1$ is enriched in O, updating the core boundary coordinate to encompass m_{k-1} , and mixing the C extruded into zone $k-2$ outward until stability is re-established. We continue iterating outward and advancing the core boundary through N_{cr} zones until reaching a point where $\phi_{k-N_{\text{cr}}} < \phi_{\text{sep}}$ so that zone $k-N_{\text{cr}}$ is outside the crystallization boundary at the end of the time step. After cooling for another time step, the process of phase separation will then start again from the location of the saved value of m_{cr} . This ensures that no material that is already in the solid phase undergoes further separation into an even more O-enriched composition as long as cooling is monotonic.

Figure 3 shows how the C/O profiles change over the course of crystallization and phase separation in a MESA model for a $0.6 M_{\odot}$ WD using the algorithm described in this section. As the WD evolves, the outer boundary of the crystallized core advances outward from the center toward the surface until eventually encountering the He envelope. We allow phase separation to proceed until reaching a location where $X_{C/O} < 0.9$. Once C and O are no longer the dominant elements, we do not expect pure C/O phase diagrams to be valid, so we do not allow C/O phase separation to proceed beyond that point. The overall change to the composition profile seen in Figure 3 is similar to what is seen in other WD codes that implement similar phase diagrams for C/O

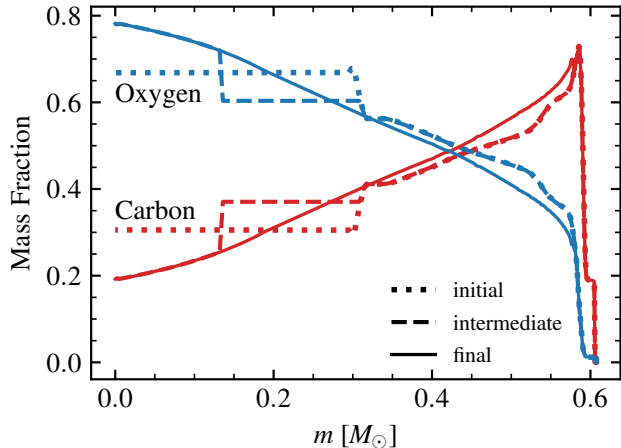


Figure 3. Carbon and oxygen profiles before, during, and after phase separation in a $0.6 M_{\odot}$ WD model.

crystallization, e.g. the LPCODE models of Althaus et al. (2012) that use the phase diagram of Horowitz et al. (2010).

3.3. Phase Separation Heating

As seen in Figure 3, the net result of phase separation is to transport some O toward the center of the model while pushing some C out toward the surface. This mixing changes the structure and binding energy of the WD interior, resulting in a heating term that introduces a cooling delay in addition to the latent heat released by crystallization. We account for this heating term in the MESA model by making EOS calls that return the internal energy of each zone before and after the composition changes due to phase separation during a timestep. That is, for internal energy $e(\rho, T, \{X_i\})$ from the Skye EOS, the heating term from phase separation in zone k is calculated over a timestep δt as

$$\epsilon_k = \frac{e(\rho_{k,\text{start}}, T_k, \{X_i\}_{k,\text{start}}) - e(\rho_{k,\text{end}}, T_k, \{X_i\}_{k,\text{end}})}{\delta t}, \quad (8)$$

where $\{X_i\}_{k,\text{start}}$ is the set of mass fractions representing the composition of zone k at the beginning of the step, and $\{X_i\}_{k,\text{end}}$ is the composition after phase separation has modified the composition of zone k . The temperature T_k is held fixed at the start-of-step value during the phase separation procedure, while ρ_k experiences small changes due to the composition adjustments at constant pressure P_k . The heating term ϵ_k from phase separation is then included as a source term in the energy equation as part of the subsequent stellar structure solution for the MESA timestep.

4. WHITE DWARF COOLING

We now demonstrate the effects of our implementation of C/O phase separation on MESA WD cooling models. In order to make these WD cooling models and comparisons, we

construct two sets of C/O WD starting models over the mass range $0.5 - 1.0 M_{\odot}$. The first set of models descends from prior MESA stellar evolution calculations, while the second set adopts a simple parameterized composition with 50% C and 50% O by mass throughout the WD core for comparison to a common set of assumptions in the historical literature. These two sets of models are motivated by the fact that the best constraints for C/O ratios in WD interiors remain both theoretically and observationally uncertain. Historically, the simplest assumption in the face of this uncertainty has been to adopt a 50/50 C/O ratio (e.g., Fontaine et al. 2001), and many WD phase separation calculations have adopted this assumption. Stellar evolution models generally produce interior compositions that are somewhat more rich in O than C, but the exact ratio is sensitive to reaction rates as well as the details of core convection during He burning (e.g., Straniero et al. 2003). Our MESA WD models descended from prior stellar evolution calculations in this work have central O mass fractions of roughly $0.6 - 0.7$, which is generally representative of the range of C/O ratios produced by stellar evolution codes for standard $^{12}\text{C}(\alpha, \gamma)^{16}\text{O}$ rates. For more detail including composition profiles, see Appendix A.

We construct our set of WD models descended from full 1D stellar evolution calculations using the MESA test suite case `make_co_wd`. These models start from the pre-main sequence and evolve through interior hydrogen and helium burning up to the first thermal pulse, after which the envelope is stripped to leave a hydrogen-rich shell of $10^{-3} M_{\odot}$. Residual hydrogen burning and element diffusion then allow the models to settle onto the WD cooling sequence as DA WDs with pure hydrogen envelopes of mass $\approx 10^{-5} - 10^{-4} M_{\odot}$ depending on the underlying WD mass. We achieve final WD masses in the range $0.5 - 1.0 M_{\odot}$ from initial MS masses of $\approx 2.5 - 6.5 M_{\odot}$. We save these starting WD models when they have cooled to a luminosity of $1 L_{\odot}$, near the beginning of the WD cooling sequence. More information about these WD models can be found in Appendix A.

For comparisons to other codes and phase separation calculations, our second set of models adopts a simplified interior C/O composition profile that is precisely 50% carbon and 50% oxygen by mass throughout the interior, with a $10^{-2} M_{\odot}$ He envelope and a $10^{-4} M_{\odot}$ H envelope surrounding the C/O core. We construct these models using the MESA tool `wd_builder`³ to build a $0.6 M_{\odot}$ model, and then we rescale to other masses using the MESA `relax_mass_scale` procedure, which scales a model to a different total mass

³ This tool was developed by Josiah Schwab and is now part of the MESA-contrib repository (<https://github.com/MESAHub/mesa-contrib>). It allows constructing MESA WD initial models that specify an arbitrary composition and high entropy, rather than constructing them through prior stellar evolution.

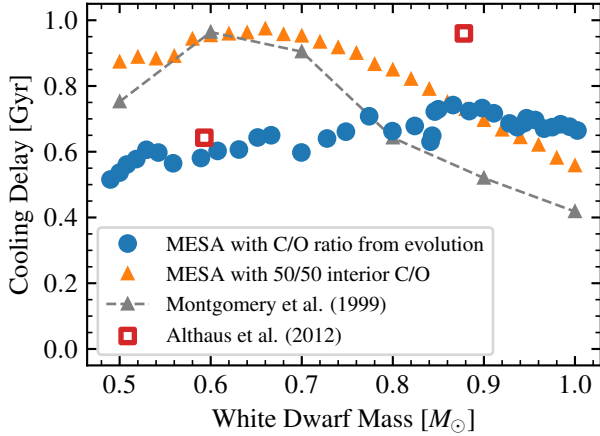


Figure 4. Cooling delays as a function of WD mass. The gray points and curve are from figure 8 of [Montgomery et al. \(1999\)](#) (lower panel, curve a), which uses the azeotropic phase diagram of [Ichimaru et al. \(1988\)](#). The red squares are from the models of [Althaus et al. \(2012\)](#), which use the phase diagram of [Horowitz et al. \(2010\)](#)

while keeping the composition profile as a function of fractional mass coordinate fixed. For simplicity, we set the parameter `eps_nuc_factor` to 0 in these models so that energy generated by nuclear burning in the hydrogen envelope does not lead to instability when scaling to higher WD mass, since an H envelope mass of $10^{-4} M_{\odot}$ is unstable on a WD more massive than $0.6 M_{\odot}$ (e.g., [Romero et al. 2019](#)). Without energy generated by nuclear burning, however, the hydrogen envelope in more massive WDs simply burns down to its most massive stable configuration at the very beginning of the cooling sequence, so these WD models have what is often referred to as “thick” hydrogen envelopes while avoiding unphysical amounts of hydrogen for massive WDs. We refer to these models throughout this paper as “50/50 C/O” models.

4.1. Phase Separation Cooling Delay

Our WD cooling calculations use these sets of WD starting models, evolving from an initial luminosity of $1 L_{\odot}$ and cooling until they reach a luminosity of $2 \times 10^{-5} L_{\odot}$. Interior crystallization and phase separation takes place completely between these two luminosities for all C/O WD masses considered here, and so the total difference in cooling age to reach a luminosity of $2 \times 10^{-5} L_{\odot}$ between models with and without phase separation quantifies the total cooling delay produced by C/O phase separation.

All our WD cooling models use the atmosphere boundary conditions of [Rohrmann et al. \(2012\)](#) appropriate for DA WDs, and the interior thermodynamics are governed by the Skye EOS ([Jermyn et al. 2021, 2023](#)). This EOS includes

the latent heat of crystallization calculated self-consistently from the local thermodynamics as described in the previous sections, and this term is included for all models both with and without phase separation.⁴ For simplicity in the models in this section, we do not include heavy element (e.g., ^{22}Ne) sedimentation, which can introduce an independent cooling delay of comparable magnitude to that from phase separation ([Bildsten & Hall 2001](#); [García-Berro et al. 2008](#), see Section 5). For conductive opacities, all MESA models shown in this section apply the [Blouin et al. \(2020b\)](#) correction factors to the [Cassisi et al. \(2007\)](#) opacities. Appendix B discusses some uncertainties in conductive opacities and shows their impact on the overall cooling delays associated with phase separation in our MESA models. We run cooling calculations twice for each WD starting model, with and without phase separation, and the difference in cooling age to reach the final luminosity therefore represents the total cooling delay produced by phase separation, independent from sedimentation or latent heat.

Figure 4 shows the total net cooling delay from C/O phase separation for both of our grids of WD models. For comparison, the figure also includes the cooling delays calculated by [Montgomery et al. \(1999\)](#) for WD models with 50/50 C/O interiors when using the azeotropic phase diagram of [Ichimaru et al. \(1988\)](#), which is the most qualitatively similar to our adopted C/O phase diagram ([Blouin et al. 2020a](#); [Blouin & Daligault 2021a](#)) out of the diagrams explored by [Montgomery et al. \(1999\)](#). Our set of 50/50 C/O MESA models shows qualitative agreement with these results of [Montgomery et al. \(1999\)](#) that use similar composition input and assumptions. Our models that descend from full evolutionary calculations show a different trend for cooling delay as a function of mass, and notably show more variation for small mass changes due to being descended from different progenitors rather than having smoothly rescaled overall mass with fixed composition profiles. Figure 4 also shows delays from the LPCODE models of [Althaus et al. \(2012\)](#), which have interior C/O profiles descended from full evolutionary calculations similar to our MESA models. These LPCODE models employ the phase diagram of [Horowitz et al. \(2010\)](#), which is quite similar to the higher-resolution phase diagram of [Blouin et al. \(2020a\)](#). Our MESA models therefore yield very similar overall cooling delays to those seen in the LPCODE, and the differences seen in Figure 4 are almost entirely due to our choice of conductive opacities (see Appendix B for

⁴ Most WD evolutionary codes implement an approximate latent heating term of $0.77 k_B T / \langle A \rangle m_p$ based on the averaged calculations of [Salaris et al. \(2000\)](#). [Baiko \(2023\)](#) has recently shown that the magnitude of the latent heat in C/O mixtures can vary by up to $\approx \pm 30\%$ from the [Salaris et al. \(2000\)](#) value depending on C/O ratio. Our models using Skye can dynamically capture this variation as the C/O ratio evolves in models experiencing phase separation.

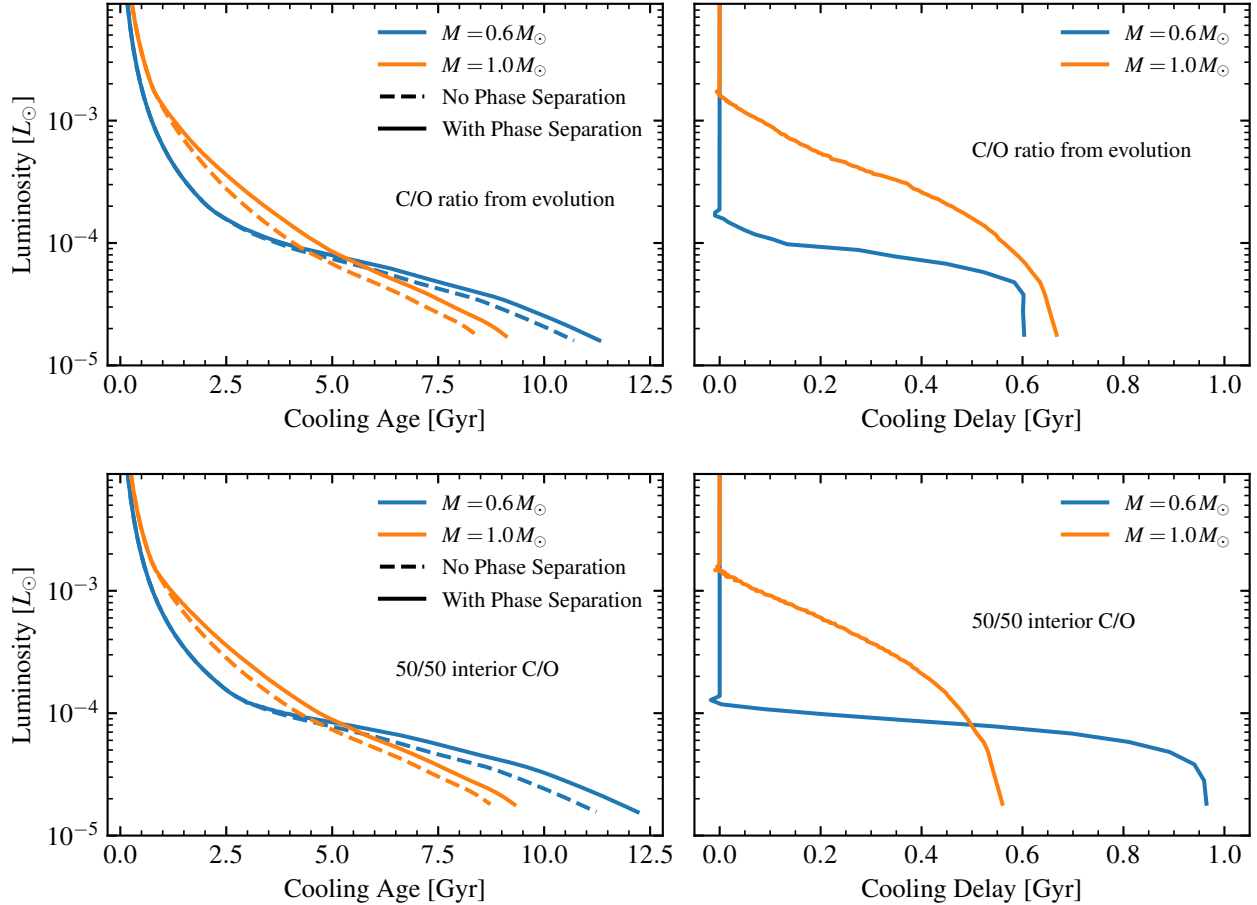


Figure 5. White dwarf cooling tracks and associated phase separation cooling delays for a variety of MESA WD cooling models. The upper panels show MESA models with internal composition profiles produced by detailed prior evolutionary calculations, while the lower panels show MESA models that adopt a simplified internal C/O composition that is exactly 50% C and 50% O by mass.

more detail and MESA models that use the same conductive opacities as the LPCODE models).

For a typical $\approx 0.6M_{\odot}$ WD, the phase separation cooling delay is substantially shorter for a model with a C/O composition produced by prior stellar evolution calculations than for a 50/50 C/O model. In this case, the details of the phase diagram happen to maximize the impact of phase separation on cooling timescales at a C/O ratio around 50/50, while more O-rich C/O ratios result in a somewhat more modest amount of total separation and cooling delay. So even though 50/50 C/O would appear to be a simple and agnostic choice of C/O ratio, it may tend to exaggerate the overall impact of phase separation on cooling timescales. For more massive C/O WDs, the delays become more similar due to an overall decreasing trend of the delays with mass for the 50/50 C/O models.

Figure 5 provides more detailed evolutionary tracks demonstrating the accumulation of the phase separation cooling delay for $0.6M_{\odot}$ and $1.0M_{\odot}$ models. The upper panels show delays for models with C/O compositions from evo-

lutionary calculations, while the lower panels show models with 50/50 C/O interiors. The $1.0M_{\odot}$ models appear to continue accumulating a small amount of cooling delay even at very low luminosities, but this delay is not due to ongoing phase separation. It is rather due to phase separation having adjusted the interior composition profile enough that fully crystallized WD models simply have slightly different thermodynamics and cooling rates even after phase separation has completed.

4.2. Comparisons to Other Codes

As a benchmark to compare our MESA WD cooling implementation to other commonly used WD cooling tracks, we plot MESA cooling tracks for $0.6M_{\odot}$ DA WD models in Figure 6. To facilitate comparisons with other codes that implement alternative electron conductive opacities, we include both a track that uses only the [Cassisi et al. \(2007\)](#) conductive opacities as well as a track that includes the [Blouin et al. \(2020b\)](#) corrections. We show comparisons to cooling tracks from the Montreal STELUM “thick envelope”

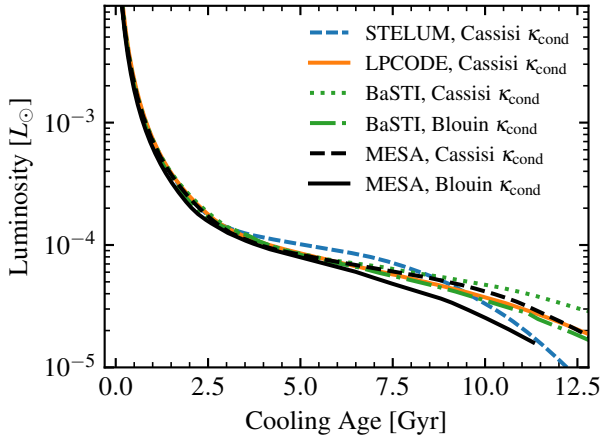


Figure 6. Comparison of cooling tracks for $0.6 M_{\odot}$ DA WD models from MESA and three other codes. The STELUM track is from Bédard et al. (2020), the LPCODE track is from Althaus et al. (2015), and the BaSTI tracks are from Salaris et al. (2022).

model grid (Bédard et al. 2020), the LPCODE WD models for low-metallicity progenitors (Althaus et al. 2015), and the BaSTI WD model grid (Salaris et al. 2022). The STELUM and LPCODE models both use the uncorrected Cassisi et al. (2007) conductive opacities only. The BaSTI grid of models provides tracks for the uncorrected Cassisi et al. (2007) conductive opacities as well tracks for models that include the Blouin et al. (2020b) corrections, so we include one of each for the BaSTI models. In all cases, we have selected the option for WDs descended from low-metallicity progenitors so that ^{22}Ne sedimentation has no impact on the cooling timescales for any of the models shown in this section (^{22}Ne in WD interiors descends from the primordial CNO abundances of a WD progenitor star).

The STELUM models (Bédard et al. 2020, 2022) are very widely used as a reference for WD cooling timescales, but the widely used model tracks that are published online⁵ make a number of simplifying assumptions that are not ideal for accurate WD cooling at late times. Unlike the other models in this section, the STELUM models use gray Eddington atmosphere boundary conditions rather than tabulated outer boundaries that account for non-gray radiative transfer such as those of Rohrmann et al. (2012). These models also assume flat 50/50 interior C/O ratio by mass, and while STELUM does include options for C/O phase separation (Bédard et al. 2022), the public tracks based on Bédard et al. (2020) do not include any C/O phase separation upon crystallization. Therefore, the STELUM cooling track in Figure 6 does not agree well with MESA or the other WD

codes at low luminosities and temperatures. MESA models can closely recover the STELUM cooling track by selecting options to emulate all of the above simplifying assumptions.

The LPCODE model (Althaus et al. 2015)⁶ in Figure 6 includes very similar input physics assumptions to the MESA model: they both use the same tabulated DA atmosphere boundary conditions (Rohrmann et al. 2012) and very similar interior C/O composition profiles produced by prior stellar evolution models. The LPCODE model employs the phase diagram of Horowitz et al. (2010) for crystallization and phase separation, which is very similar to the Blouin & Dalgault (2021a) phase diagram employed by MESA (Blouin et al. 2020a). Reassuringly, the MESA model that makes the same assumption about conductive opacities matches the LPCODE cooling track very closely.

The BaSTI models (Salaris et al. 2022) make very similar assumptions to the models of both MESA and LPCODE in terms of atmosphere boundary conditions, interior composition profiles, phase diagram, and phase separation. However, they exhibit much slower cooling after crystallization, and we speculate that this is due to differences in the thermodynamics of the solid phase reported by their choice of EOS.

5. RELATION TO NEON SEDIMENTATION

In degenerate WD interiors, hydrostatic equilibrium establishes an electric field that approximately balances gravity for the dominant ion species C and O (Bildsten & Hall 2001; Chang et al. 2010). The net force experienced by ion species i is $F_i = -A_i m_p g + Z_i e E$, with $e E \approx 2 m_p g$, which approximately cancels for the dominant background, while ions with extra neutrons ($A_i > 2Z_i$) such as ^{22}Ne and ^{23}Na experience a net downward force that can lead to sedimentation (Bauer et al. 2020). ^{22}Ne in particular is present in WD interiors at a mass fraction that reflects the initial metallicity Z of their progenitor stars, as CNO burning results in most of the core metallicity becoming ^{14}N by the end of the main sequence, which then burns to ^{22}Ne during the He burning that forms the C/O WD core.

Heavy-element sedimentation causes heating that can slow WD cooling (Isern et al. 1991; Bildsten & Hall 2001; Deloye & Bildsten 2002), with the magnitude of this effect scaling up with WD progenitor metallicity, and this has been implemented and studied in several WD evolution codes (García-Berro et al. 2008; Paxton et al. 2018; Bauer et al. 2020; Salaris et al. 2022). This cooling delay operates in addition to any delay from crystallization and phase separation, and

⁵ <https://www.astro.umontreal.ca/~bergeron/CoolingModels/>

⁶ This paper includes models from several different progenitors with low metallicity, and we select the track from the $Z = 3 \times 10^{-5}$ model for the comparison here. The other models in Althaus et al. (2015) have a significant extra cooling delay at earlier times due to residual hydrogen burning, but that effect is negligible in the $Z = 3 \times 10^{-5}$ model.

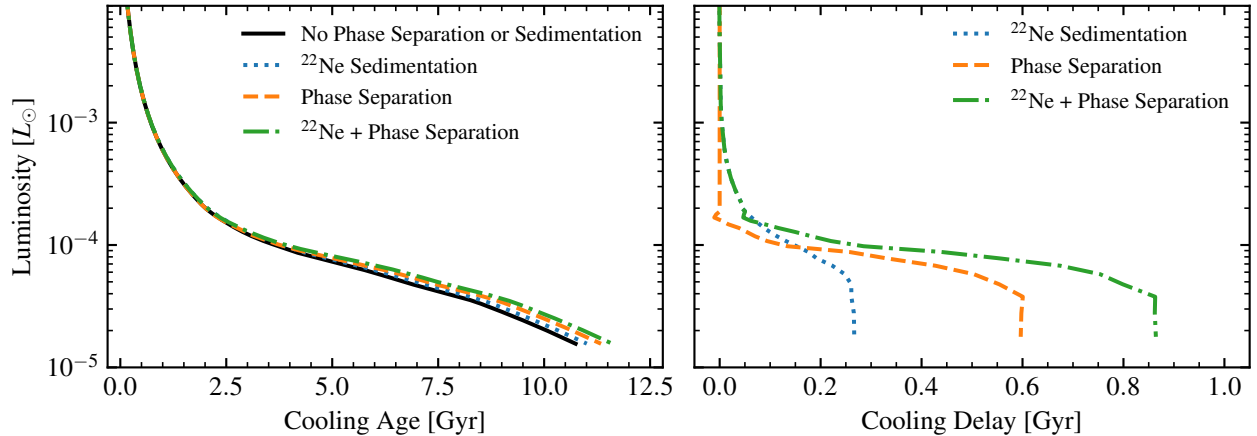


Figure 7. WD cooling delays associated with both phase separation and ^{22}Ne sedimentation for a $0.6M_{\odot}$ DA WD model.

in particular the confluence of these two delays has been invoked to explain the slow cooling of the WD population in the metal-rich ($Z \approx 0.04$) open cluster NGC 6791 (García-Berro et al. 2010; Althaus et al. 2010). In this section we consider MESA models in which both phase separation and heavy-element sedimentation processes operate, and compare to the delays seen in other WD codes.

Our models in this section all descend from $Z = 0.02$ progenitors, so that the interior mass fraction of ^{22}Ne is roughly 0.02 throughout the C/O core. We include element diffusion in the liquid portion of the WD core following the treatment described in Paxton et al. (2018); Bauer et al. (2020); Jermyn et al. (2023), with a smooth turnoff of diffusion in the crystallized solid regions according to the smoothed phase parameter ϕ introduced in previous sections. The diffusion coefficients in the strongly-coupled plasma of the WD core are those of Caplan et al. (2022), which closely match the coefficients of Hughto et al. (2010) that are often used for ^{22}Ne sedimentation in WDs.

Figure 7 shows cooling tracks and associated cooling delays for models with and without both ^{22}Ne sedimentation heating and C/O phase separation. Our baseline model includes element diffusion but not phase separation, and omits the heating term associated with heavy-element sedimentation. Our second model turns on this heating term, which is responsible for the modest ≈ 0.3 Gyr delay seen in the dotted blue curve. Our third model turns this sedimentation heating back off while turning on phase separation, resulting in a somewhat more substantial delay of ≈ 0.6 Gyr seen in the dashed orange curve. Our final model turns on both of these effects together to yield a total delay of ≈ 0.9 Gyr. This verifies that our implementations of both these effects in MESA are compatible with each other and lead to the expected total delay from both independent processes.

With our implementation of sedimentation including state-of-the-art diffusion coefficients (Caplan et al. 2022), our WD cooling delays from ^{22}Ne sedimentation are significantly shorter than those seen in LPCODE models of C/O WDs at the same metallicity (Camisassa et al. 2016), regardless of whether C/O phase separation is considered. This is despite having implementations of other WD cooling physics including crystallization and phase separation that very closely match other aspects of the LPCODE models (see Figure 6). LPCODE models of C/O WDs at $Z = 0.02$ exhibit ^{22}Ne cooling delays greater than 1 Gyr according to Camisassa et al. (2016). In contrast, our MESA models show a delay of only 0.3 Gyr, and recent BaSTI models that include ^{22}Ne sedimentation also show a relatively modest delay of ≈ 0.5 Gyr for $0.6M_{\odot}$ WDs descended from $Z = 0.02$ progenitors (Salaris et al. 2022). The original implementation of ^{22}Ne sedimentation in LPCODE from García-Berro et al. (2008) also showed much more modest cooling delays when employing their default ^{22}Ne diffusion coefficient based on Deloye & Bildsten (2002). While more recent MD simulations have yielded better constraints on the diffusion coefficient (Hughto et al. 2010; Caplan et al. 2022), the overall change relative to the coefficient employed by García-Berro et al. (2008) is modest and should only result in slightly slower sedimentation, so it is not clear why more recent LPCODE models show much larger ^{22}Ne sedimentation delays (Althaus et al. 2010; Camisassa et al. 2016, 2021).

We therefore argue that the ^{22}Ne cooling delays in LPCODE models may be significantly overestimated, and this could have important implications for some inferences based on the cooling timescales of these models. LPCODE models have been used to resolve a discrepancy in the WD cooling ages for the metal-rich open cluster NGC 6791, which was originally thought to have a main sequence turnoff age more than 2 Gyr older than the age inferred from comparing the

WD luminosity function to WD cooling models (Bedin et al. 2008). García-Berro et al. (2010) used LPCODE models to argue that the inclusion of both C/O phase separation and ^{22}Ne sedimentation could provide a long enough cooling delay to resolve this discrepancy. However, the faster cooling timescales and more modest ^{22}Ne delays seen in our MESA models would reintroduce tension between the age inferred from the WD luminosity function and the ages inferred from the other stellar populations in NGC 6791.

Camisassa et al. (2021) have also recently used LPCODE models for WDs descended from very metal-rich progenitors ($Z = 0.06$) to argue that ^{22}Ne sedimentation could explain the anomalous observed kinematics for some Q -branch WDs, interpreted as evidence of an ≈ 8 Gyr cooling delay for some massive WDs (Cheng et al. 2019). However, since MESA models show less than half the cooling delay compared to LPCODE models for a given amount of ^{22}Ne sedimentation, an explanation invoking standard sedimentation alone would require an implausibly high ^{22}Ne abundance corresponding to $Z \gtrsim 0.15$ if our MESA models are accurate.

While heavy-element sedimentation alone is likely insufficient to explain the cooling delays in either NGC 6791 or the Q -branch WDs, the recently proposed process of ^{22}Ne “distillation” (Blouin et al. 2021) is a promising avenue for explaining these delays by enhancing transport of ^{22}Ne toward the center through dynamical mixing. This process is somewhat analogous to C/O phase separation in that crystallization of a multi-component plasma induces some amount of instability and mixing, but the physics is more complicated due to requiring a three-component phase diagram rather than the simpler two-component diagram employed for C/O phase separation in this work. Still, it appears that distillation shows the most promise for explaining cooling delays in WDs descended from metal-rich ($Z \gtrsim 0.02$) populations, and may in fact be required by observations such as those of NGC 6791 and the Q -branch. Our present work with MESA lays the groundwork for future investigation of distillation based on three-component phase diagrams (Blouin et al. 2021; Caplan et al. 2023) in full WD evolutionary models.

6. CONCLUSIONS

We have provided a new implementation of C/O phase separation during WD crystallization as part of the publicly available stellar evolution software MESA. Our implementation relies on the phase diagram of Blouin & Daligault (2021a), and produces a net transport of O toward the center and C toward the surface. This rearrangement of the interior chemical profile during WD crystallization provides an energy source that can delay WD cooling. In our detailed MESA models, the net cooling delay is typically on the order of 0.5 Gyr. This is somewhat smaller than often quoted

delays of ≈ 1 Gyr, which can arise from older phase diagrams that led to more dramatic separation in typical WD models, or from models that assume core C and O mass fractions of exactly 0.5, where the phase diagram happens to maximize the impact of separation. Our WD models descended from MESA models of prior stellar evolution have central O mass fractions of roughly 0.6–0.7 depending on mass.

Our models that include C/O phase separation show good agreement with other WD models that implement comparable physics, such as the LPCODE models of Althaus et al. (2012, 2015). However, there is tension in the overall WD cooling timescales between MESA and LPCODE WD cooling models that implement comparable physics with both C/O phase separation and heavy-element sedimentation for WDs descended from metal-rich ($Z \gtrsim 0.02$) progenitor populations. If the cooling timescales of our MESA models are correct, this may reintroduce discrepancies between WDs associated with observed metal-rich populations (e.g., NGC 6791 and the Q -branch) and state-of-the-art WD cooling models that include the most up-to-date input physics. This would then require the implementation of newly proposed pieces of input physics to resolve these discrepancies, such as distillation in three-component mixtures (Blouin et al. 2021). Our progress with MESA in this work lays the groundwork for future investigations to explore these new physical processes with detailed WD evolution models.

Acknowledgments: EB gratefully acknowledges helpful conversations with Simon Blouin, María Camisassa, Charlie Conroy, Bart Dunlap, Mike Montgomery, and Alejandra Romero during the development of this work. EB is also grateful to the anonymous referee for helpful suggestions improving both the text and figures for the key results of this work. EB also thanks the MESA developers team for building and maintaining the open software upon which this work rests, especially Adam Jermyn and Josiah Schwab for developing the particular capabilities leveraged by this work. This work benefited from discussions at the KITP program *White Dwarfs as Probes of the Evolution of Planets, Stars, the Milky Way and the Expanding Universe* in the Fall of 2022, and was supported in part by the National Science Foundation under Grant No. NSF PHY-1748958.

Software: MESA (Paxton et al. 2011, 2013, 2015, 2018, 2019; Jermyn et al. 2023), Skye (Jermyn et al. 2021), matplotlib (Hunter 2007), NumPy (van der Walt et al. 2011), and Python from python.org.

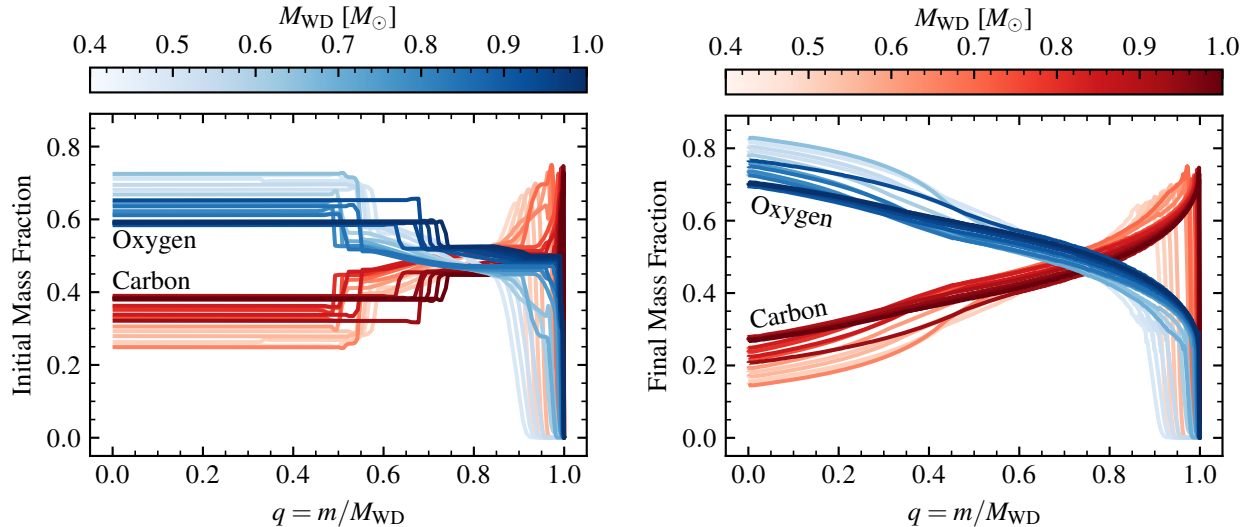


Figure 8. Carbon and oxygen composition profiles versus fractional mass coordinate $q = m/M_{\text{WD}}$ for our MESA WD models with masses in the range $0.5 - 1.0 M_{\odot}$, before (left) and after (right) C/O phase separation. Darker line colors indicate more massive WD models. For the right panel, “after” phase separation is defined as having reached a point where the C/O-dominated layers have completely crystallized, so that no further mixing due to phase separation will occur.

APPENDIX

A. WHITE DWARF MODELS

Figure 8 shows the C/O composition profiles from a representative subset of our WD models descended from full prior stellar evolution calculations. We use MESA to evolve our models from ZAMS through H and He burning up to the point of the first thermal pulse on the AGB. Once the first thermal pulse occurs, we artificially strip the outer envelope and turn on diffusion to allow the models to settle onto the WD cooling sequence with pure H atmospheres as DA WDs. Since this step of the process circumvents realistic AGB mass loss, it does not produce an accurate initial-to-final mass relation (IFMR), but it does produce a representative range of C/O profiles in the interior core region where burning has ceased, so this is sufficient for our study in this work. The starting interior C/O ratio produced by evolution prior to the WD stage is sensitive to the $^{12}\text{C}(\alpha, \gamma)^{16}\text{O}$ reaction rate (Fields et al. 2016; deBoer et al. 2017; Chidester et al. 2022). We adopt the Kunz et al. (2002) rate for this reaction for our models in this work, which is quite similar to the deBoer et al. (2017) rate for the temperature range relevant for He core and shell burning to produce WD interior C/O profiles. Our MESA WD models show core O mass fractions in the range $\approx 0.6 - 0.75$, with the lower-mass models typically on the more O-rich end in their interiors. The low-mass models also tend to have very thick He envelopes of up to about $0.05 M_{\odot}$, but the He envelope masses are thinner than $10^{-2} M_{\odot}$ for typical WD masses around $0.6 M_{\odot}$, and as thin as $10^{-3} M_{\odot}$ for the most massive WDs around $1.0 M_{\odot}$.

While the interior C/O composition profiles of our MESA models are generally representative of the current state of the art for 1D stellar evolution models, we feel it is also worth noting that significant uncertainty remains as to the precise interior composition and especially the ratio of C to O in WD cores. Helium burning generically coincides with α captures onto ^{12}C to produce a mixture of C and O, but uncertainty in the $^{12}\text{C}(\alpha, \gamma)^{16}\text{O}$ reaction rate makes it difficult to predict the precise ratios from 1D stellar evolution calculations (deBoer et al. 2017; De Gerónimo et al. 2017, 2019; Chidester et al. 2022). It has been suggested that WD asteroseismology could be used to constrain interior structure and composition of WD models, and ultimately may even yield constraints on the $^{12}\text{C}(\alpha, \gamma)^{16}\text{O}$ reaction rate as a result (Metcalf et al. 2001, 2002; Fontaine & Brassard 2002; Metcalfe 2003). Indeed, some recent studies have attempted to use seismology to constrain WD interior compositions (Giammichele et al. 2018; Charpinet et al. 2019; Giammichele et al. 2022), yielding central O mass fractions as high as 0.86, which would be difficult to produce with reasonable assumptions in 1D stellar evolution models (De Gerónimo et al. 2019). However, Timmes et al. (2018) and Chidester et al. (2021) have pointed out some additional pieces of physics that are not accounted for in the parameterized

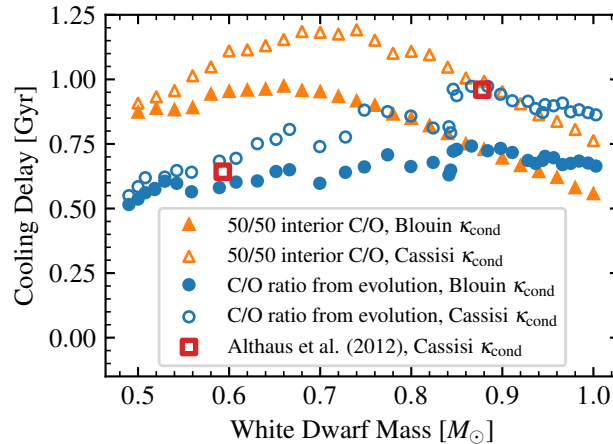


Figure 9. Cooling delays as a function of WD mass, similar to Figure 4, but including models with different conductive opacities. Open symbols represent models using only the conductive opacities of Cassisi et al. (2007), while filled symbols represent models that include the corrections of Blouin et al. (2020b).

models used for the Giammichele et al. (2018) fitting procedure, and including these extra effects on the structure can shift the mode frequencies beyond the quoted uncertainties of the models. Bell (2022) also recently showed that the Giammichele et al. (2018); Charpinet et al. (2019) fits for the WD KIC 08626021 are inconsistent with the astrometry from *Gaia*, suggesting that the seismological fitting procedure may be overly flexible and yield much larger uncertainties than currently appreciated. Some other recent WD seismology studies have pointed out that pulsation spectra are far more sensitive to other aspects of WD structure such as composition transition locations and shapes, making it difficult to confidently isolate a pulsation signal firmly constraining the central C/O mass fractions (e.g., Bischoff-Kim et al. 2019; Bell et al. 2019).

B. CONDUCTIVE OPACITIES

The current default treatment of conductive opacities in MESA applies correction factors to the classic values of Cassisi et al. (2007) based on the recent calculations of Blouin et al. (2020b). However, Blouin et al. (2020b), Cassisi et al. (2021), and Salaris et al. (2022) have all pointed out that there is still substantial uncertainty in how best to bridge between the regimes of moderate and strong electron degeneracy for conductive opacities. WD models typically cool faster at late times when applying the Blouin et al. (2020b) conductive opacity corrections, which can decrease the effective opacity by a factor of 2-3 in some regimes (Blouin et al. 2020b; Salaris et al. 2022; Jermyn et al. 2023). Figure 9 shows phase separation cooling delays for MESA models that use the Cassisi et al. (2007) opacities without any corrections, alongside the models from Section 4 that include the corrections from Blouin et al. (2020b). While the qualitative trends are similar in either case, the overall cooling delays associated with crystallization and phase separation are somewhat shorter when applying the Blouin et al. (2020b) opacities because of the overall faster cooling for these models. The LPCODE models from Althaus et al. (2012) employ the Cassisi et al. (2007) conductive opacities as well, and agree very well with our models that use the same conductive opacities. As the focus of the current work is simply to describe our implementation of phase separation and quantify its effects, we withhold judgment on which set of conductive opacities offers more accurate absolute WD cooling timescales, and emphasize that MESA makes either set of opacities easily available to those who wish to explore further.

REFERENCES

- Althaus, L. G., Camisassa, M. E., Miller Bertolami, M. M., Córscico, A. H., & García-Berro, E. 2015, *A&A*, 576, A9
- Althaus, L. G., García-Berro, E., Isern, J., Córscico, A. H., & Miller Bertolami, M. M. 2012, *A&A*, 537, A33
- Althaus, L. G., García-Berro, E., Renedo, I., et al. 2010, *ApJ*, 719, 612
- Angulo, C., Arnould, M., Rayet, M., et al. 1999, *Nuclear Physics A*, 656, 3
- Baiko, D. A. 2023, *MNRAS*, 522, L26
- Bauer, E. B., Schwab, J., Bildsten, L., & Cheng, S. 2020, *ApJ*, 902, 93

- Bédard, A., Bergeron, P., Brassard, P., & Fontaine, G. 2020, *ApJ*, 901, 93
- Bédard, A., Brassard, P., Bergeron, P., & Blouin, S. 2022, *ApJ*, 927, 128
- Bedin, L. R., King, I. R., Anderson, J., et al. 2008, *ApJ*, 678, 1279
- Bell, K. J. 2022, *Research Notes of the American Astronomical Society*, 6, 244
- Bell, K. J., Córscico, A. H., Bischoff-Kim, A., et al. 2019, *A&A*, 632, A42
- Belloni, D., Schreiber, M. R., Salaris, M., Maccarone, T. J., & Zorotovic, M. 2021, *MNRAS*, 505, L74
- Bildsten, L., & Hall, D. M. 2001, *ApJL*, 549, L219
- Bischoff-Kim, A., Provencal, J. L., Bradley, P. A., et al. 2019, *ApJ*, 871, 13
- Blouin, S., & Daligault, J. 2021a, *PhRvE*, 103, 043204
- . 2021b, *ApJ*, 919, 87
- Blouin, S., Daligault, J., & Saumon, D. 2021, *ApJL*, 911, L5
- Blouin, S., Daligault, J., Saumon, D., Bédard, A., & Brassard, P. 2020a, *A&A*, 640, L11
- Blouin, S., Shaffer, N. R., Saumon, D., & Starrett, C. E. 2020b, *ApJ*, 899, 46
- Camisassa, M. E., Althaus, L. G., Córscico, A. H., et al. 2016, *ApJ*, 823, 158
- Camisassa, M. E., Althaus, L. G., Torres, S., et al. 2021, *A&A*, 649, L7
- Caplan, M. E., Bauer, E. B., & Freeman, I. F. 2022, *MNRAS*, 513, L52
- Caplan, M. E., Blouin, S., & Freeman, I. F. 2023, arXiv e-prints, arXiv:2303.03409 [astro-ph.SR]
- Caplan, M. E., Horowitz, C. J., & Cumming, A. 2020, *ApJL*, 902, L44
- Cassisi, S., Potekhin, A. Y., Pietrinferni, A., Catelan, M., & Salaris, M. 2007, *ApJ*, 661, 1094
- Cassisi, S., Potekhin, A. Y., Salaris, M., & Pietrinferni, A. 2021, *A&A*, 654, A149
- Chang, P., Bildsten, L., & Arras, P. 2010, *ApJ*, 723, 719
- Charpinet, S., Brassard, P., Giammichele, N., & Fontaine, G. 2019, *A&A*, 628, L2
- Cheng, S., Cummings, J. D., & Ménard, B. 2019, *ApJ*, 886, 100
- Chidester, M. T., Farag, E., & Timmes, F. X. 2022, *ApJ*, 935, 21
- Chidester, M. T., Timmes, F. X., Schwab, J., et al. 2021, *ApJ*, 910, 24
- Chugunov, A. I., Dewitt, H. E., & Yakovlev, D. G. 2007, *PhRvD*, 76, 025028
- Cyburt, R. H., Amthor, A. M., Ferguson, R., et al. 2010, *ApJS*, 189, 240
- De Gerónimo, F. C., Althaus, L. G., Córscico, A. H., Romero, A. D., & Kepler, S. O. 2017, *A&A*, 599, A21
- De Gerónimo, F. C., Battich, T., Miller Bertolami, M. M., Althaus, L. G., & Córscico, A. H. 2019, *A&A*, 630, A100
- deBoer, R. J., Görres, J., Wiescher, M., et al. 2017, *Reviews of Modern Physics*, 89, 035007
- Deloye, C. J., & Bildsten, L. 2002, *ApJ*, 580, 1077
- Ferguson, J. W., Alexander, D. R., Allard, F., et al. 2005, *ApJ*, 623, 585
- Fields, C. E., Farmer, R., Petermann, I., Iliadis, C., & Timmes, F. X. 2016, *ApJ*, 823, 46
- Fontaine, G., & Brassard, P. 2002, *ApJL*, 581, L33
- Fontaine, G., Brassard, P., & Bergeron, P. 2001, *PASP*, 113, 409
- Fuentes, J. R., Cumming, A., Castro-Tapia, M., & Anders, E. H. 2023, arXiv e-prints, arXiv:2301.04273 [astro-ph.SR]
- Fuller, G. M., Fowler, W. A., & Newman, M. J. 1985, *ApJ*, 293, 1
- García-Berro, E., Althaus, L. G., Córscico, A. H., & Isern, J. 2008, *ApJ*, 677, 473
- García-Berro, E., Torres, S., Althaus, L. G., et al. 2010, *Nature*, 465, 194
- Giammichele, N., Charpinet, S., & Brassard, P. 2022, *Frontiers in Astronomy and Space Sciences*, 9, 879045
- Giammichele, N., Charpinet, S., Fontaine, G., et al. 2018, *Nature*, 554, 73
- Ginzburg, S., Fuller, J., Kawka, A., & Caiazzo, I. 2022, *MNRAS*, 514, 4111
- Horowitz, C. J., & Caplan, M. E. 2021, *PhRvL*, 126, 131101
- Horowitz, C. J., Schneider, A. S., & Berry, D. K. 2010, *PhRvL*, 104, 231101
- Hughto, J., Schneider, A. S., Horowitz, C. J., & Berry, D. K. 2010, *PhRvE*, 82, 066401
- Hunter, J. D. 2007, *Computing In Science & Engineering*, 9, 90
- Ichimaru, S., Iyetomi, H., & Ogata, S. 1988, *ApJL*, 334, L17
- Iglesias, C. A., & Rogers, F. J. 1993, *ApJ*, 412, 752
- . 1996, *ApJ*, 464, 943
- Irwin, A. W. 2004, *The FreeEOS Code for Calculating the Equation of State for Stellar Interiors*
- Isern, J., García-Berro, E., Külebi, B., & Lorén-Aguilar, P. 2017, *ApJL*, 836, L28
- Isern, J., Hernanz, M., Mochkovitch, R., & Garcia-Berro, E. 1991, *A&A*, 241, L29
- Isern, J., Mochkovitch, R., García-Berro, E., & Hernanz, M. 1997, *ApJ*, 485, 308
- Itoh, N., Hayashi, H., Nishikawa, A., & Kohyama, Y. 1996, *ApJS*, 102, 411
- Jermyn, A. S., Schwab, J., Bauer, E., Timmes, F. X., & Potekhin, A. Y. 2021, *ApJ*, 913, 72
- Jermyn, A. S., Bauer, E. B., Schwab, J., et al. 2023, *ApJS*, 265, 15
- Kunz, R., Fey, M., Jaeger, M., et al. 2002, *ApJ*, 567, 643
- Langanke, K., & Martínez-Pinedo, G. 2000, *Nuclear Physics A*, 673, 481
- Medin, Z., & Cumming, A. 2010, *PhRvE*, 81, 036107
- Mestel, L. 1952, *MNRAS*, 112, 583
- Metcalf, T. S. 2003, *ApJL*, 587, L43

- Metcalf, T. S., Salaris, M., & Winget, D. E. 2002, *ApJ*, 573, 803
- Metcalf, T. S., Winget, D. E., & Charbonneau, P. 2001, *ApJ*, 557, 1021
- Mochkovitch, R. 1983, *A&A*, 122, 212
- Montgomery, M. H., Klumpe, E. W., Winget, D. E., & Wood, M. A. 1999, *ApJ*, 525, 482
- Oda, T., Hino, M., Muto, K., Takahara, M., & Sato, K. 1994, *Atomic Data and Nuclear Data Tables*, 56, 231
- Ogata, S., Iyetomi, H., Ichimaru, S., & van Horn, H. M. 1993, *PhRvE*, 48, 1344
- Paxton, B., Bildsten, L., Dotter, A., et al. 2011, *ApJS*, 192, 3
- Paxton, B., Cantiello, M., Arras, P., et al. 2013, *ApJS*, 208, 4
- Paxton, B., Marchant, P., Schwab, J., et al. 2015, *ApJS*, 220, 15
- Paxton, B., Schwab, J., Bauer, E. B., et al. 2018, *ApJS*, 234, 34
- Paxton, B., Smolec, R., Schwab, J., et al. 2019, *ApJS*, 243, 10
- Potekhin, A. Y., & Chabrier, G. 2010, *Contributions to Plasma Physics*, 50, 82
- Poutanen, J. 2017, *ApJ*, 835, 119
- Rogers, F. J., & Nayfonov, A. 2002, *ApJ*, 576, 1064
- Rohrman, R. D., Althaus, L. G., García-Berro, E., Córscico, A. H., & Miller Bertolami, M. M. 2012, *A&A*, 546, A119
- Romero, A. D., Kepler, S. O., Joyce, S. R. G., Lauffer, G. R., & Córscico, A. H. 2019, *MNRAS*, 484, 2711
- Salaris, M., Cassisi, S., Pietrinferni, A., & Hidalgo, S. 2022, *MNRAS*, 509, 5197
- Salaris, M., García-Berro, E., Hernanz, M., Isern, J., & Saumon, D. 2000, *ApJ*, 544, 1036
- Saumon, D., Chabrier, G., & van Horn, H. M. 1995, *ApJS*, 99, 713
- Schreiber, M. R., Belloni, D., Gänsicke, B. T., & Parsons, S. G. 2021a, *MNRAS*, 506, L29
- Schreiber, M. R., Belloni, D., Gänsicke, B. T., Parsons, S. G., & Zorotovic, M. 2021b, *Nature Astronomy*, 5, 648
- Schreiber, M. R., Belloni, D., Zorotovic, M., et al. 2022, *MNRAS*, 513, 3090
- Segretain, L., & Chabrier, G. 1993, *A&A*, 271, L13
- Stevenson, D. J. 1977, *PASA*, 3, 167
- Straniero, O., Domínguez, I., Imbriani, G., & Piersanti, L. 2003, *ApJ*, 583, 878
- Timmes, F. X., & Swesty, F. D. 2000, *ApJS*, 126, 501
- Timmes, F. X., Townsend, R. H. D., Bauer, E. B., et al. 2018, *ApJL*, 867, L30
- van der Walt, S., Colbert, S. C., & Varoquaux, G. 2011, *Computing in Science Engineering*, 13, 22
- van Horn, H. M. 1968, *ApJ*, 151, 227
- Winget, D. E., Hansen, C. J., Liebert, J., et al. 1987, *ApJL*, 315, L77
- Winget, D. E., Kepler, S. O., Campos, F., et al. 2009, *ApJL*, 693, L6